Plasmonic nanomesh sandwiches for ultrathin film silicon solar cells

Tongchuan Gao[1], Baomin Wang[2] and Paul W Leu[1]

[1] Department of Industrial Engineering, University of Pittsburgh, Pittsburgh, PA 15261, USA
[2] Department of Electrical Engineering, The Pennsylvania State University, University Park, PA 16802, USA

E-mail: pleu@pitt.edu

CrossMark

Abstract

We theoretically investigate the strategy of integrating metal nanoparticles (NPs)/nanomeshes (NMs) into the top and/or bottom of crystalline silicon (c-Si) thin film solar cells for light trapping and enhanced carrier collection. C-Si thin films exhibit absorption resonances corresponding to Fabry–Pérot modes. Frontside metal NPs enhance absorption by additionally coupling light into localized surface plasmon resonances and c-Si waveguide modes, while a frontside metal NM increases absorption by coupling light into surface plasmon polaritons and c-Si waveguide modes. The frontside metal NM also functions as a flexible top electrode, which may replace conventional brittle transparent conductive oxide thin films. The backside metal NM exhibits enhanced absorption due to the coupling of light into c-Si waveguide modes and the cavity modes within the holes of metal NM. We illustrate how the optimal metal NM sandwich, consisting of NMs on both sides of a 300 nm thick c-Si with an appropriate antireflection coating (ARC), achieves a 72.9% enhancement in short-circuit current density compared with that of a 300 nm thick c-Si thin film solar cell with 100 nm thick Si_3N_4 ARC and 300 nm thick Ag back reflector. The current generation in the metal NM sandwich is more in the center of the thin film such that there should be less surface recombination. The uniform current generation throughout the film results in less overall recombination.

Keywords: light trapping, photovoltaics, nanosphere lithography, metal nanomesh, ultrathin film solar cells, plasmonics

(Some figures may appear in colour only in the online journal)

1. Introduction

Crystalline silicon (c-Si) is the prevailing solar cell material due to Si's non-toxic nature, high crust abundance, and nearly ideal band gap for solar energy conversion. However, c-Si is an indirect band gap material such that solar cells are typically several hundred microns thick to ensure high spectral absorption. This results in expensive material costs not only from the amount of material, but from high purity requirements to ensure good collection of photogenerated carriers. Thin film solar cells have emerged as an alternative to reduce material costs and may be suitable for incorporation into low-cost and flexible substrates [1–6]. In thin film solar cells, light trapping is important for ensuring high absorption within little photoactive material. Thin film solar cells with light trapping

may also have larger open circuit voltages and fill factors due to suppressed Auger recombination from less material. Research on light trapping has been burgeoning in the past decade, with both theoretical studies on the limit of absorption enhancement in weak absorbers [7, 8] and experimental demonstrations of a myriad of strategies. Various structures have been shown to increase the light absorption in the photoactive region, such as surface texturing [9, 10], plasmonic metal nanostructures [11–19], and dielectric nanospheres [20–22].

Plasmonic nanostructures have been theoretically and experimentally demonstrated as effective light trapping elements for solar cells to increase optical absorption and thus cell efficiency. Theoretical study has focused on the principles for tailoring subwavelength metal nanostructures to maximize

the light absorption in c-Si thin films with a thickness ranging from 100 to 300 nm [13, 19, 21, 23]. Most work has focused on the use of metal nanoparticles (NPs) for light trapping [11–14]. Metal NPs are strong scatterers of light, especially near their localized surface plasmon resonance (LSPR) frequencies, which are used to scatter light preferentially into the photoactive region [15–18]. Periodic metal NP arrays are used to enhance the absorption in thin film c-Si by the coupling of incident light into TE and TM waveguide modes in the c-Si and the excitation of LSPRs [13]. Apart from metal NPs, a variety of continuous metal nanostructures have also been shown to plasmonically trap light in c-Si solar cells. For example, metal gratings on the top of the structure can couple light to waveguide modes and LSPRs [19]. Nanostructured back reflectors enhance photocurrent by exciting Fabry–Pérot and waveguide modes [24–26]. Moreover, a variety of scalable and affordable fabrication methods have been established accordingly. It is noteworthy that the top electrode is an important component of a thin film solar cell, which has a significant impact on the overall efficiency of the solar cell. Reflection, absorption, and resistive losses in top electrode may reduce the solar cell efficiency by 10%–25% [27]. Recently, we demonstrated the scalable fabrication of nanomeshes (NMs) or metal NPs using microsphere or nanosphere lithography [28, 29]. These structures are suitable for being incorporated into solar cells as top electrodes and/or efficient scatters of light.

In this paper, we report on numerical investigations of the optical absorption and short-circuit current densities of ultrathin c-Si solar cells with the incorporation of metal NPs or NMs into the top and/or bottom of the c-Si. The properties for the c-Si thin film with an antireflection coating (ARC) and/or a flat back reflector as well as an ideal double pass c-Si thin film are simulated for benchmarking. The results are compared with the properties for ultrathin c-Si solar cells with metal NPs/NM on either side. We demonstrate that metal NMs may function as both a plasmonic light trapping element and a transparent top electrode when deposited on the top side of the ultrathin c-Si film, and as effective back reflector when placed on the back side. A variety of metals, including Ag, Au, Cu, Al, and Ni, have been used to investigate the plasmonic effects when contacting dielectrics [30–32]. In this paper, we studied the effect of nanostructured Al and Ag for ultrathin c-Si solar cells, because Au introduce states near the middle of the Si band gap that serve as highly effective recombination centers, and Cu diffuses rapidly into c-Si even at room temperature. Our results shed light on the design principles of these structures for improved c-Si solar cell performance.

2. Methods

Figure 1(a) illustrates schematics of the four types of systems studied: ultrathin c-Si film with (i) frontside metal NM/NPs, (ii) backside metal NM, (iii) metal NM sandwich, and (iv) metal NM sandwich with ARC. The parameters for the various systems studied are illustrated in figure 1(b). The

photoactive region consists of an ultrathin c-Si film with thickness t_{Si}. The metal NMs are metal thin films with holes in a hexagonal array. The top NM is defined by the pitch a_{top}, hole diameter d_{top}, and metal thickness t_{top}. The bottom NM is defined by the pitch a_{bot}, hole diameter d_{bot}, and metal thickness t_{bot}. For simplicity, we assume the top and bottom pitch are equal, $a_{top} = a_{bot} = |\vec{a_1}| = |\vec{a_2}|$. The thickness of the ARC is t_{ARC}, and the x and y component of the off-shift between the top and bottom NM lattice are denoted by u and v respectively (not shown in the schematic). As a proof-of-concept, we investigate ultrathin c-Si film with $t_{Si} = 300$ nm and metal NMs with pitch $a_{top} = a_{bot} = a = 200$–1000 nm, and hole diameter d_{top} and $d_{bot} = 200$–1000 nm, where d_{top} and $d_{bot} \leqslant a$.

We performed electrodynamic simulations to determine the optical properties of solar cells by solving Maxwell's equations using the finite-difference time-domain (FDTD) method [33, 34]. We used a perfectly matched layer as the top and bottom boundary condition to truncate the simulation super cell. The side boundary conditions of the supercell are set to be antisymmetric and symmetric in the direction of the electric and magnetic field respectively to model the periodic nature of the metal NMs. We also utilized a non-uniform simulation mesh with a finer mesh near interfaces and larger mesh in bulk regions. The optical constants for the c-Si, Ag, and Al are taken from experimental results in Palik's *Handbook of Optical Constants of Solids* [35] and the refractive indices for silicon nitride are taken from [36].

The position dependent absorption per unit volume $A(\mathbf{r}, \lambda)$ is calculated from the divergence of the Poynting vector $\mathbf{P}$:

$$A(\mathbf{r}, \lambda) = \frac{1}{2}\text{real}\{\vec{\nabla} \cdot \mathbf{P}\} = \frac{1}{2}\epsilon_i(\lambda)\omega(\lambda)|\mathbf{E}(\mathbf{r}, \lambda)|^2, \quad (1)$$

where λ is the free-space wavelength, $\epsilon_i(\lambda)$ is the imaginary part of the permittivity, $\omega(\lambda) = 2\pi c/\lambda$ is the photon angular frequency, c is the speed of light, and $\mathbf{E}(\mathbf{r}, \lambda)$ is the electric field vector as the function of position and wavelength. The absorption spectra $A(\lambda)$ of the Si photoactive region is obtained by integrating the position dependent absorption per unit volume over the Si volume, $A(\lambda) = \int A(\mathbf{r}, \lambda) dV_{Si}$. This eliminates any parasitic absorption that may occur in the metal that does not contribute to solar efficiency. Assuming that each absorbed photon generates one electron–hole pair, and that all photogenerated carriers are collected, the short-circuit current density is

$$J_{sc} = q \int_0^{\lambda_g} I(\lambda) A(\lambda) \frac{\lambda}{\lambda_g} d\lambda. \quad (2)$$

$\lambda_g = 1107$ nm is the free-space wavelength corresponding to the band gap of c-Si ($E_g = 1.12$ eV), and $I(\lambda)$ is the solar irradiance under the global 37° tilt Air Mass 1.5 spectrum [37]. We use the FDTD method to determine the transmission of the frontside NM as the transparent electrode, and the finite element method to simulate the sheet resistance R_s by solving the transport equation. The resistivity of bulk metals is assumed in these simulations. Solar integrated transmission is
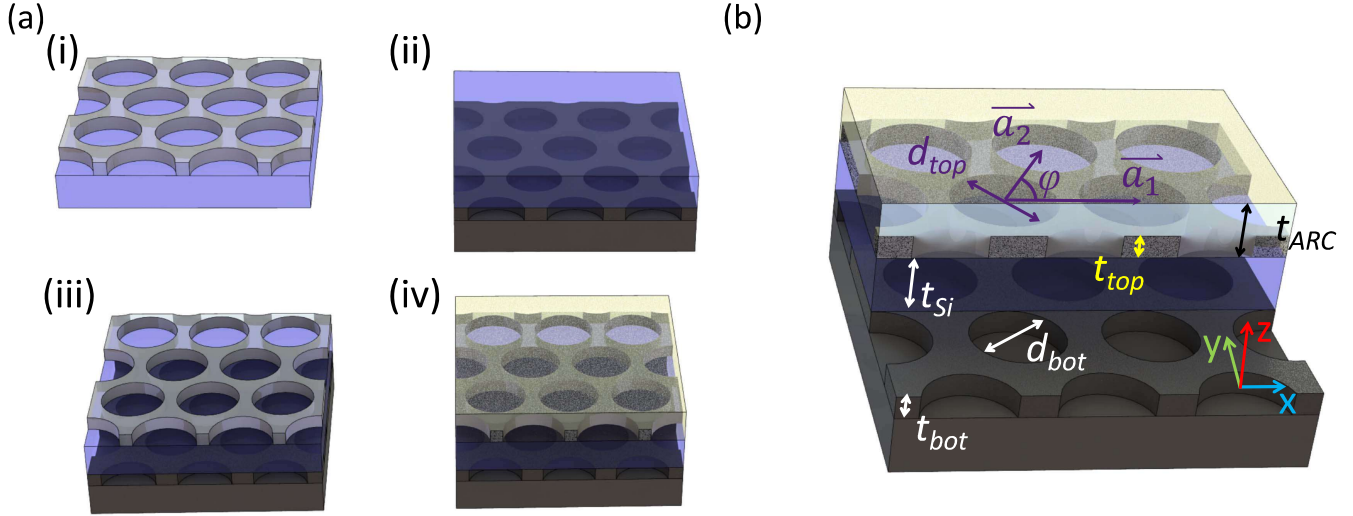
Figure 1. Schematics of the plasmonic solar cell structures studied, including (a) ultrathin c-Si film with (i) frontside metal NM or NPs, (ii) backside metal NM, (iii) metal NM sandwich, and (iv) metal NM sandwich with antireflection coating and backside metal. (b) Parameters of the various structures studied.

calculated from

$$T_{\text{solar}} = \frac{\int b(\lambda) T(\lambda) \mathrm{d}\lambda}{\int b(\lambda) \mathrm{d}\lambda}, \tag{3}$$

where $b(\lambda)$ is the photon flux density under the global 37° tilt Air Mass 1.5 spectrum, and $T(\lambda)$ is the wavelength dependent optical transmission. To compare different geometries, we utilize the angle-averaged short-circuit current density $J_{\text{sc}} = (J_{\text{sc},xx} + J_{\text{sc},yy})/2$, where $J_{\text{sc},xx}$ and $J_{\text{sc},yy}$ are the short-circuit-current density under illumination polarized in the x- and y-directions respectively. Similarly, we calculate the angle-averaged sheet resistance $R_{\text{s}} = (R_{\text{s},xx} + R_{\text{s},yy})/2$, and angle-averaged transmission $T_{\text{solar}} = (T_{\text{solar},xx} + T_{\text{solar},yy})/2$, where $R_{\text{s},xx}$ and $R_{\text{s},yy}$ are the sheet resistances measured in the x- and y-direction; $T_{\text{solar},xx}$ and $T_{\text{solar},yy}$ are the transmission results under illumination polarized in the x- and y-directions, respectively.

3. Results and discussion

We first demonstrate ultrathin c-Si films with various ARC and/or back reflectors. Five structures are selected for reference, including bare c-Si film, c-Si thin film with 100 nm thick Si_3N_4 as ARC, c-Si with 300 nm thick Ag back reflector, c-Si with both ARC and Ag back reflector, and ideal double pass 300 nm thick c-Si. The short-circuit current densities are $J_{\text{sc}} = 6.0$, 7.1, 8.6, 9.4, and 11.0 mA cm^{-2}, respectively. Figure 2 shows the absorption spectra for three of these scenarios for benchmarking. The absorption near the band gap is weak due to the indirect band gap of c-Si, though multiple peaks are observed in the absorption spectra due to the Fabry–Pérot resonance supported by thin film systems. In addition, the absorption of a double pass c-Si film is calculated by

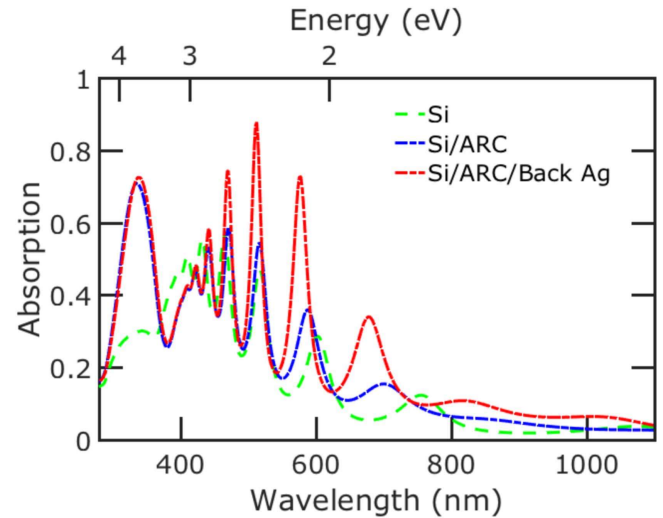$$A(\lambda) = 1 - \exp[2\alpha(\lambda) t_{\text{Si}}], \tag{4}$$

Figure 2. Absorption spectrum for 300 nm thick bare c-Si, c-Si with 100 nm Si_3N_4 ARC, and c-Si with ARC and Ag back reflector.

Table 1. The short circuit current density J_{sc} of different ultrathin Si structures.

Structure	J_{sc} (mA cm^{-2})
Si/ARC	7.1
Si/Ag back reflector	8.6
Si/ARC/Ag back reflector	9.4
Double pass Si	11.0

where $\alpha(\lambda)$ is the wavelength dependent absorption coefficient of c-Si. The ideal double pass thin film assumes perfect antireflection at the front surface, $R(\lambda) = 0$, and perfect reflection at the back surface, $R(\lambda) = 1$. The photon optical length, the distance a photon travels in the c-Si, is exactly twice the thickness of the Si. The short-circuit current density
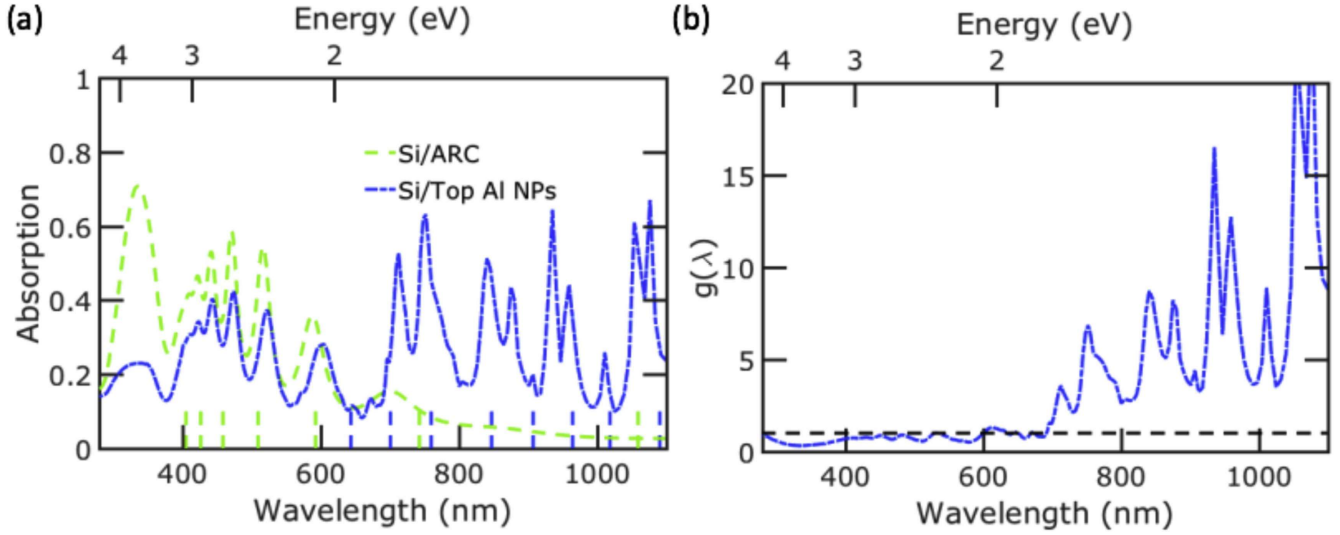
Figure 3. (a) Averaged absorption spectrum for ultrathin c-Si film with ARC and with frontside Al NPs. Fabry–Pérot and waveguide modes are plotted with green and blue dashed lines, respectively, near the *x*-axis. (b) The enhancement in optical absorption as a function of wavelength.

is $J_{sc} = 11.0$ mA cm^{-2} in this case. Table 1 summarizes the short-circuit current density results for these thin film structures.

3.1. Frontside NP/NM optimization

The optimization for metal nanostructures on the top side of bare ultrathin c-Si film with $t_{Si} = 300$ nm shows that the greatest enhancement in J_{sc} is achieved by NPs. NPs are defined by the condition $d_{top} = a_{top}$, such that the metal structures are not continuous and instead form triangular NPs. Specifically, Al NPs with $d_{top} = a_{top} = 800$ nm and $t_{top} = 200$ nm demonstrate the optimal results. The short-circuit current is $J_{sc} = 9.7$ mA cm^{-2} with $J_{sc,xx} = 11.5$ mA cm^{-2} and $J_{sc,yy} = 7.9$ mA cm^{-2}, corresponding to a 36.6% enhancement compared with ultrathin c-Si film with 100 nm thick Si$_3$N$_4$ ARC.

For a homogeneous planar dielectric layer, waveguide modes can be excited by a plane wave incident with the presence of scatters near the layer. The guided TE waveguide modes for a Si thin film satisfy

$$k_{Si} \tan\left(k_{Si} \frac{1}{2} t_{Si}\right) = k_x \tag{5}$$

and

$$k_{Si} \cot\left(k_{Si} \frac{1}{2} t_{Si}\right) = -k_x \tag{6}$$

for even and odd modes, respectively. k_{Si} and k_x are the transverse waves in the Si and air respectively, where $k_{Si} = (n_{Si}^2 k^2 - \beta^2)^{1/2}$ and $k_x = (\beta^2 - k^2)^{1/2}$. β is the propagation constant. The guided TM waveguide modes for a Si thin film satisfy

$$k_{Si} \tan\left(k_{Si} \frac{1}{2} t_{Si}\right) = n_{Si}^2 k_x \tag{7}$$

and

$$k_{Si} \cot\left(k_{Si} \frac{1}{2} t_{Si}\right) = n_{Si}^2 k_x \tag{8}$$

for even and odd modes, respectively. The waveguide conditions can be obtained by solving the transcendental equations above [38]. Incident light may couple to the guided modes, which become quasiguided or leaky in dielectrics [39], when the propagation constant matches the reciprocal lattice constant, $\beta = \frac{4\sqrt{3}\pi}{3a}\sqrt{p^2 - pq + q^2}$, where p and q are integers. Figure 3(a) plots the absorption spectra results for the optimized frontside NPs compared with just the Si thin film. Figure 3(a) plots the TEM Fabry–Pérot modes and waveguide modes up to $|p|$ and $|q| = 2$ with green and blue dashed lines, respectively, near the *x*-axis. The peak at 674 nm corresponds to a TE waveguide mode where $(p, q) = (3, -2)$, $(2, -3)$, $(-2, 3)$ or $(-3, 2)$ and the absorption peak at 935 nm is a $(3, 3)$ or $(-3, -3)$ TE waveguide mode. The mode at $\lambda = 792$ nm is a $(3, -2)$, $(2, -3)$, $(-2, 3)$ or $(-3, 2)$ TM waveguide mode. An additional mode is present at $\lambda = 875$ nm which is unaccounted for by this simple waveguide model. Peaks with over a 10-fold enhancement are observed near the band gap of c-Si as shown in figure 3(b).

Apart from Fabry–Pérot modes and waveguide modes, an LSPR is excited by the Al NPs at $\lambda = 712$ nm. The LSPR will lead to absorption enhancement in the c-Si thin film with little pitch dependence. Figure 4 shows the electric field profile at $\lambda = 712$ nm, in which the presence of the LSPR is evident, demonstrated by a strong localized field intensity near the vertices of each NP [40].

By constraining $d_{top} < a_{top}$, the NPs become a continuous NM that may additionally function as a transparent conductor. We optimized the NM and found that the greatest enhancement in J_{sc} is achieved by Al NM with $a_{top} = 800$ nm, $d_{top} = 760$ nm, and $t_{top} = 100$ nm. The short-
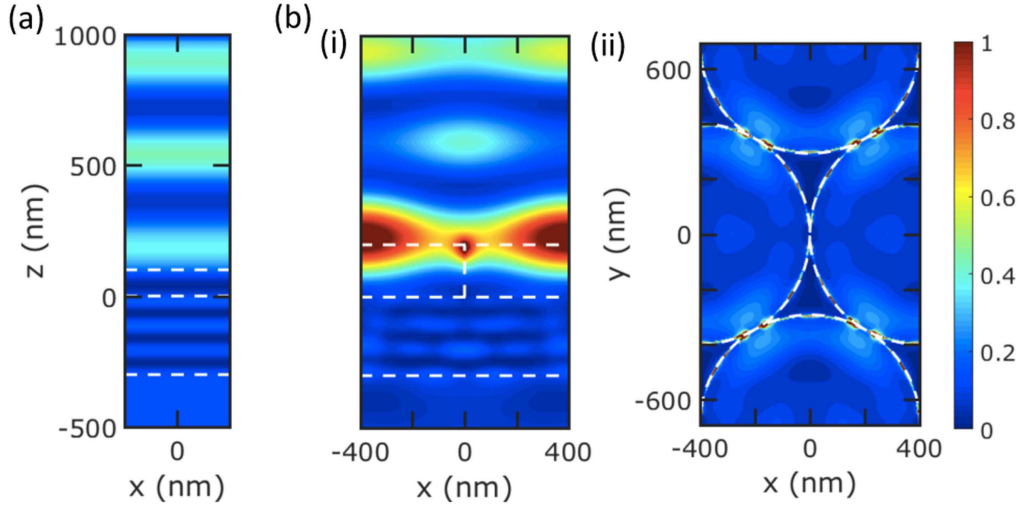
Figure 4. Normalized electric field intensity profiles at incident wavelength $\lambda = 712$ nm for (a) c-Si thin film with 100 nm ARC and (b)with frontside Al NPs. The cross-sectional view for the structure is shown in (i) the *x*–*z* plane at *y* = 0, and (ii) in the *x*–*y* plane at the Al/c-Si interface. The electric field profiles are the averaged result from incident light with polarization along *x*- and *y*-directions. The dashed white lines indicate where the c-Si film and Al NPs are located.
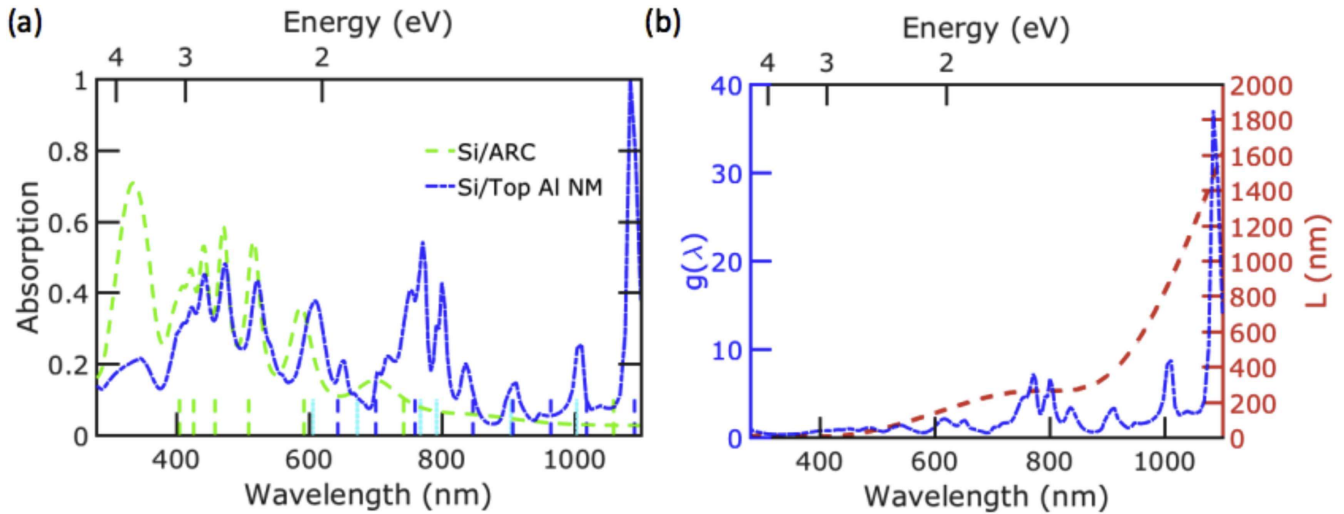

Figure 5. (a) Averaged absorption spectrum for ultrathin c-Si film with ARC and ultrathin c-Si film with frontside Al NM. Fabry–Pérot, waveguide, and SPP modes are plotted with green, blue, and cyan dashed lines, respectively, near the *x*-axis. (b) The enhancement in optical absorption $g(\lambda)$ in blue and the SPP propagation length *L* at an Al/c-Si interface as a function of wavelength in red.

circuit current is $J_{sc} = 9.6$ mA cm^{-2} with $J_{sc,xx} = 9.6$ mA cm^{-2} and $J_{sc,yy} = 9.5$ mA cm^{-2}, corresponding to a 35.2% enhancement compared with ultrathin c-Si film with ARC. The enhancement with NMs is less than that with NPs because there is more top side metal in these structures and thus more reflection and parasitic absorption. The sheet resistance averaged over the *x*- and *y*-direction is 3.2 Ω/sq at a 83% average solar transmission. Figure 5(a) plots Fabry–Pérot modes and quasiguided modes up to $|p|$ and $|q| = 2$ with green and blue dashed lines, respectively, near the *x*-axis. In addition to coupling light to waveguide modes, the NM may excite surface plasmon polaritons (SPPs). SPPs may be excited at normal incidence when the SPP wavevector

matches the reciprocal lattice constant

$$\beta_{SPP} = k \sqrt{\frac{\epsilon_{Si}\,\epsilon_m}{\epsilon_{Si} + \epsilon_m}}, \qquad (9)$$

where ϵ_m and ϵ_{Si} are the complex permittivities for metal and dielectric respectively [41]. Figure 5(a) plots SPP modes with cyan dotted lines near the *x*-axis for modes up to $|m|$ and $|n| = 3$.

The absorption enhancement is significant for incident light with larger wavelengths. A peak with over 30-fold enhancement is observed at $\lambda = 1084$ nm as shown in figure 5(b). Figure 5(b) also plots the propagation length *L* of the SPP wave at an Al/c-Si interface in red on the right *y*-axis. SPPs can be excited at the interface separating metal and
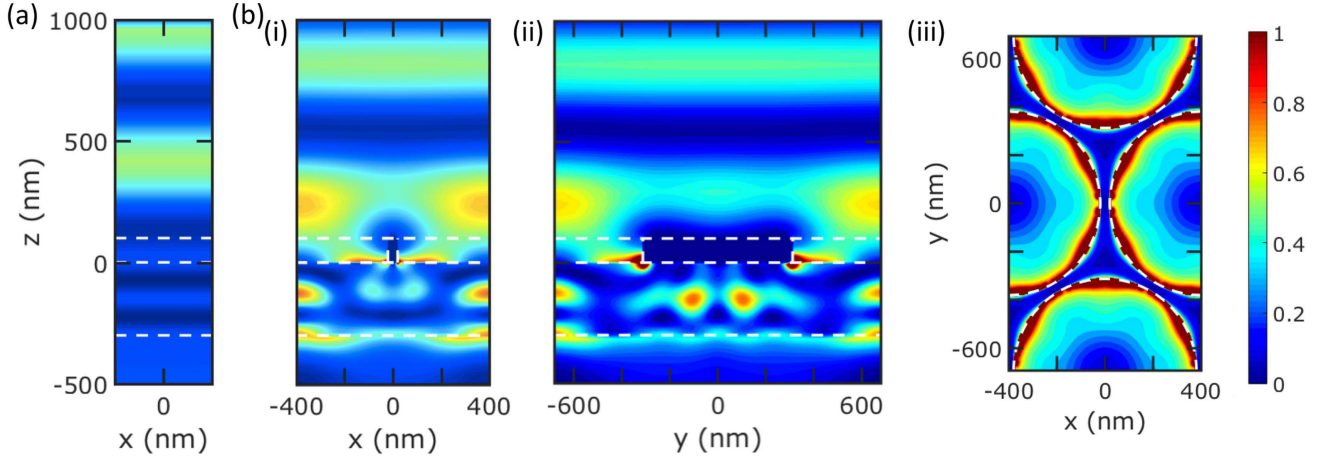
Figure 6. Normalized electric field intensity profiles at incident wavelength $\lambda = 1084$ nm for (a) bare ultrathin c-Si film and (b) ultrathin c-Si film with Al NM as transparent electrode. The cross-sectional view for the structure is shown in (i) the *x–z* plane at *y* = 0, (ii) in the *y–z* plane at *x* = 0, and (iii) in the *x–y* plane at the Al/c-Si interface. The electric field profiles are the averaged result from incident light with polarization along *x*- and *y*-directions. The dashed white lines indicate where the c-Si film and Al NM are located.
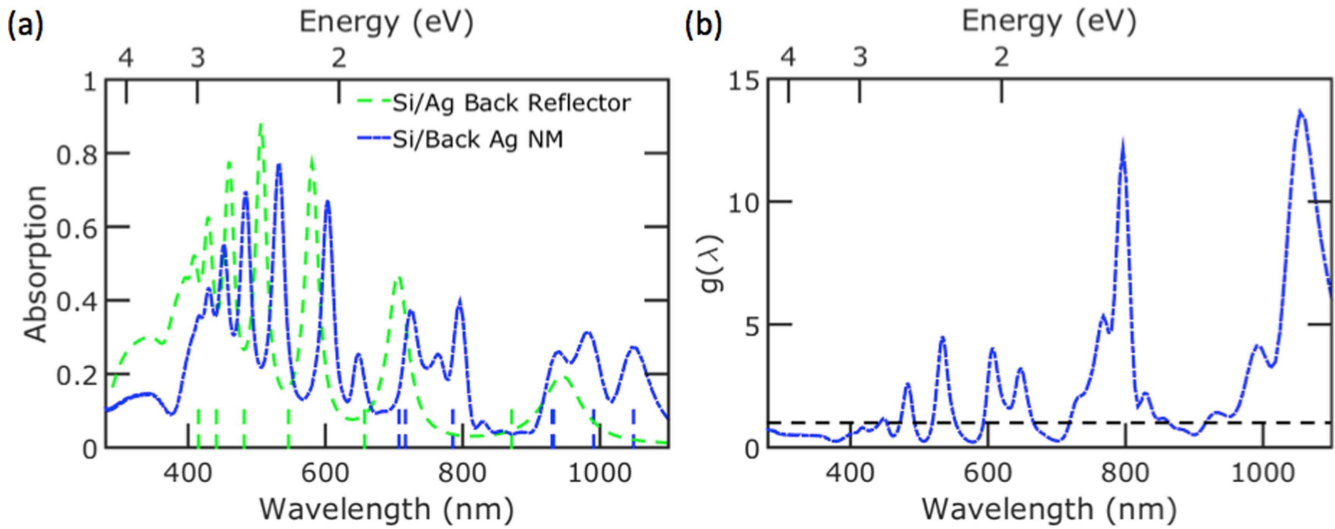

Figure 7. (a) Averaged absorption spectrum for ultrathin c-Si film with Ag film and optimal Ag NM as back reflector. Fabry–Pérot and waveguide modes are plotted with green and blue dashed lines, respectively, near the *x*-axis. (b) The enhancement of the absorption as a function of wavelength due to the Ag NM.

dielectric by the interaction between light and metal nanostructures. An SPP wave is lossy because the wave vector of SPP is greater than that of a freely propagating light at the same angular frequency ω. The traveling SPP wave at the interface attenuates exponentially with characteristic propagation length L, given by

$$L = (2 \, \text{Im}[\beta_{\text{SPP}}])^{-1}. \qquad (10)$$

SPPs decay exponentially perpendicular to the interface. Incident light with longer wavelengths excites SPPs with larger propagation length.

Figure 6 plots the electric field intensity at $\lambda = 1084$ nm. Figure 6(a) plots the electric field intensity for just the Si thin film. The field pattern at this wavelength is close to one of the Fabry–Pérot modes (the TEM$_2$ mode at $\lambda = 1059$ nm where there is a single wavelength in the transverse direction of the planar film). Figure 6(b) plots the electric field intensity with

the addition of the Al NM on top of the c-Si film in (i) the *x–z* plane at *y* = 0, (ii) in the *y–z* plane at *x* = 0, and (iii) in the *x–y* plane at the Al/c-Si interface. The electric field intensity plotted is an average for incident light polarized along the *x*- and *y*-directions. An SPP is excited with the presence of the Al NM, indicated by the enhanced electric field intensity spatially confined near the Al/c-Si interface. This corresponds to the $(1, -2)$, $(2, -1)$, $(-1, 2)$, or $(-2, 1)$ SPP mode. The coupling of incident light and the SPP results in significant light trapping and absorption enhancement in the c-Si film.

3.2. Backside NM optimization

Next, we evaluate metal NMs as effective back reflectors for ultrathin c-Si film solar cells. Specifically, we study a solar cell consisting of a $t_{\text{Si}} = 300$ nm ultrathin c-Si film with metal
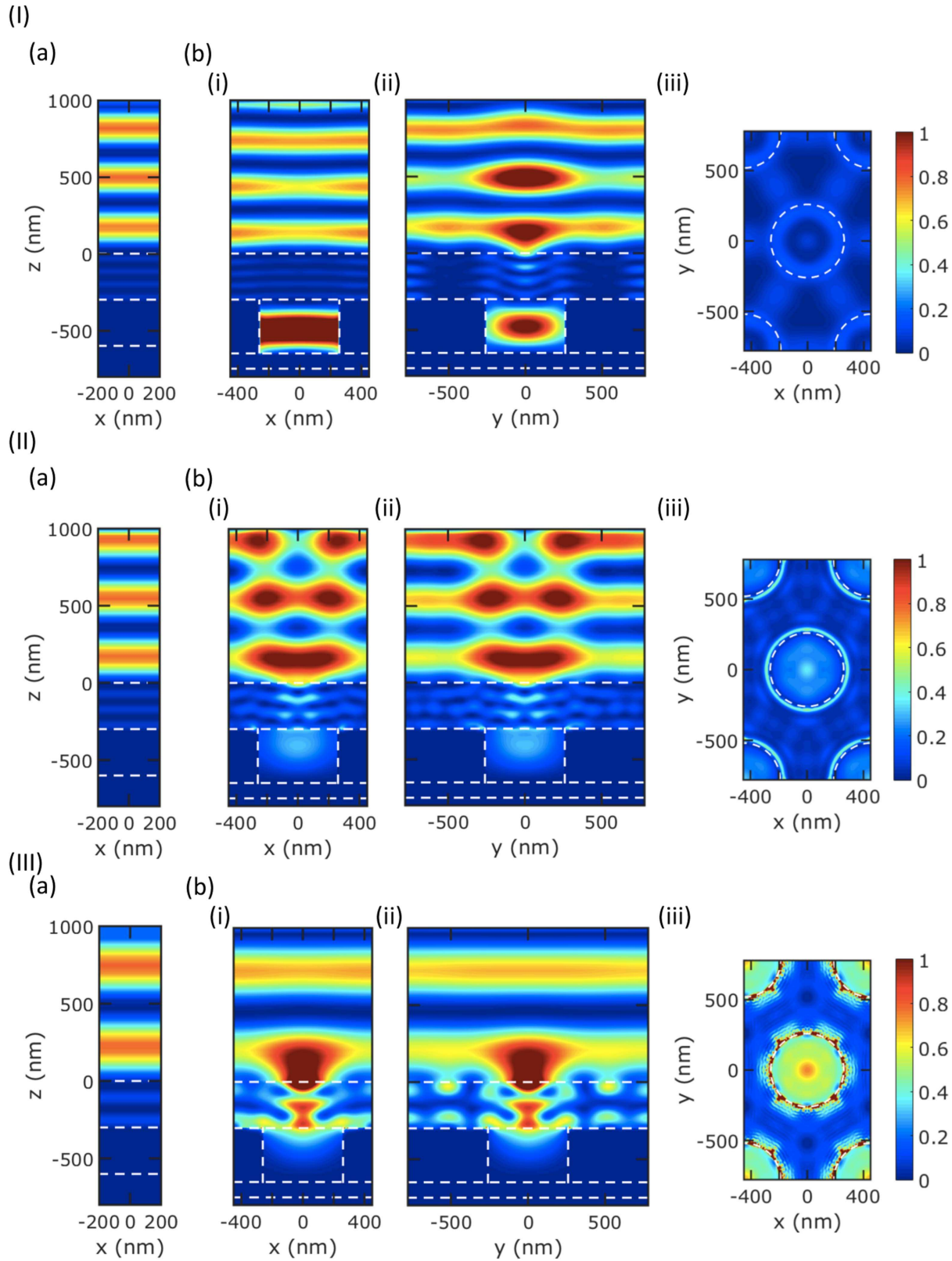
Figure 8. Normalized electric field intensity profiles at incident wavelength (I) $\lambda = 648$, (II) 764, and (III) 1046 nm for ultrathin c-Si film with (a) 300 nm Ag film and (b) optimal Ag NM as back reflector. The cross-sectional views for the structure in (i) the *x–z* plane with $y = 0$, (ii) the *y–z* plane with $x = 0$, and (iii) at the Ag NM/c-Si interface. The electric field profiles are the averaged result from incident light with polarization along *x*- and *y*-directions. The dashed white lines indicate the edges of where the c-Si thin film, Ag NM, and Ag thin film are located.
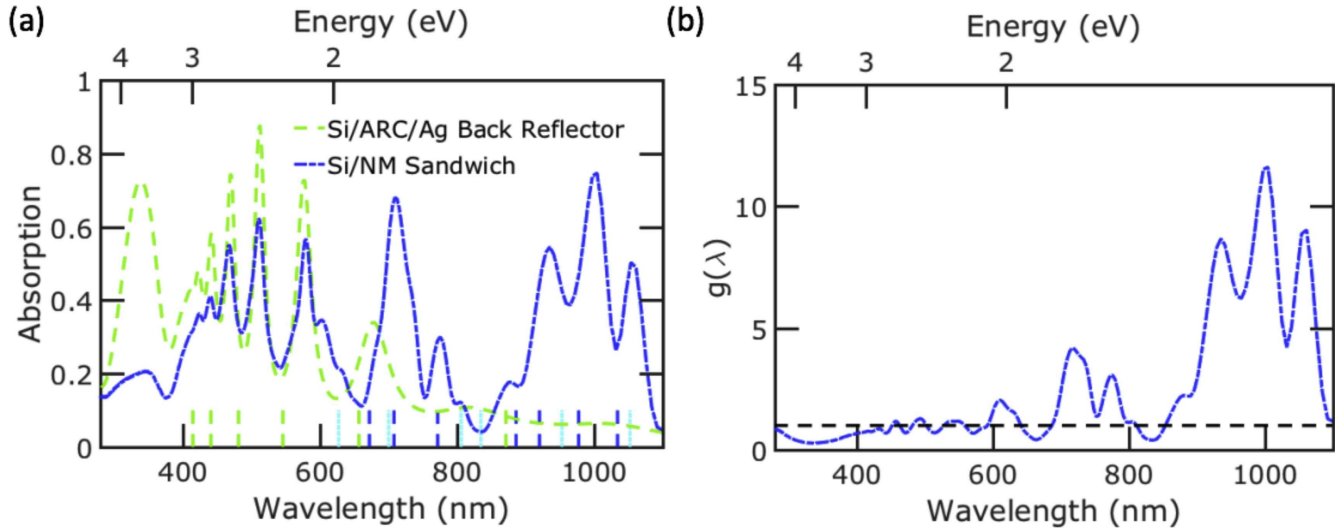
Figure 9. (a) Absorption spectrum of ultrathin c-Si film with ARC and Ag back reflector, and c-Si with the optimal NM sandwich. (b) The enhancement of the absorption as the function of wavelength.
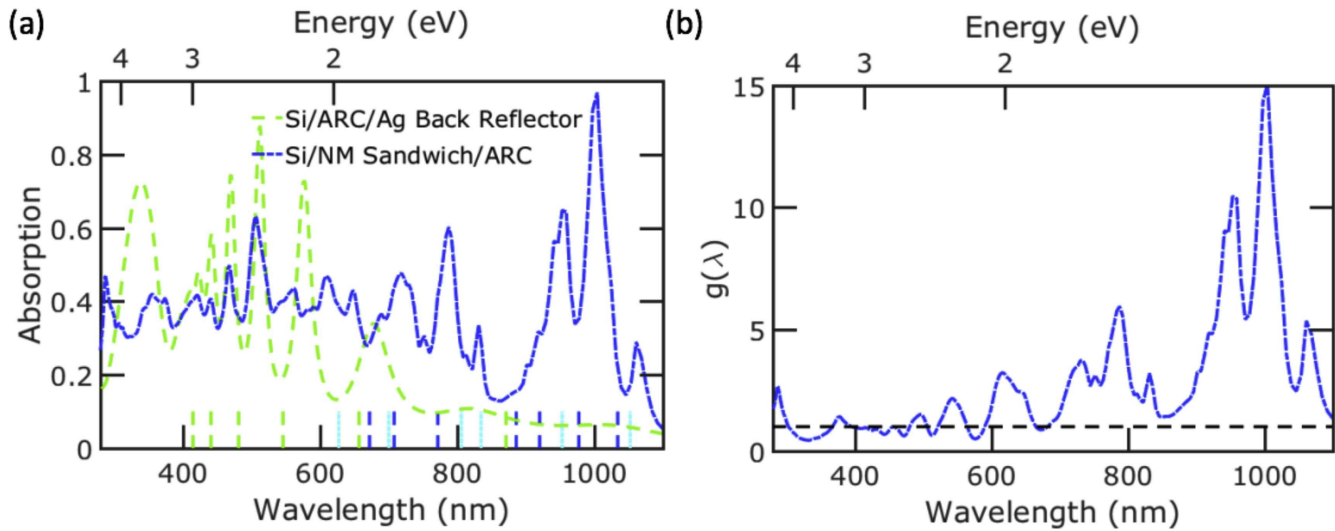

Figure 10. (a) Absorption spectrum of c-Si ultrathin film with ARC and Ag back reflector, and c-Si with the optimal double-side NMs with silicon nitride antireflection coating. (b) The enhancement of the absorption as the function of wavelength.

Table 2. The short circuit current density J_{sc} of different structures.

Structure	J_{sc} (mA cm^{-2})
Frontside NPs	9.7
Frontside NM	9.6
Backside NM	8.7
NM sandwich	13.3
NM sandwich with ARC	16.25

NM on 100 nm Ag back reflector as the backside reflector, as shown in figure 1(a)(ii). This is compared with an ultrathin c-Si film with a 300 nm Ag thin film back reflector that was discussed earlier. Figure 7(a) plots the absorption spectra for the Ag thin film back reflector and the optimized Ag NM back reflector. The optimal solar cell performance is achieved by using a backside Ag NM with $a_{bot} = 900$ nm, $d_{bot} = 520$ nm, and $t_{bot} = 350$ nm. The short-circuit current density is

$J_{sc} = 10.1$ mA cm^{-2}, with $J_{sc,xx} = 10.1$ mA cm^{-2} and $J_{sc,yy} = 10.1$ mA cm^{-2}, exhibiting a 17.4% enhancement in J_{sc} compared with c-Si thin film with a 300 nm Ag back reflector.

For shorter wavelengths, the ultrathin c-Si film with Ag NM as back reflector supports the same thin film Fabry–Pérot resonance modes as its counterpart with 300 nm Ag thin film, but with redshifted and slightly weaker absorption peaks. The redshift of the peaks arises from the larger penetration of the electromagnetic field into the Ag NM back reflector due to the leaky nature. The location of the Fabry–Pérot resonance modes are plotted near the x-axis with green dashed lines.

Leaky waveguide modes are plotted in figure 7(a) with blue dashed lines near the x-axis for modes up to $|p|$ and $|q| = 2$. These leaky waveguide modes are plotted for free-standing Si thin film without a back contact (equations (5)–(8)) since the electromagnetic field propagates into the
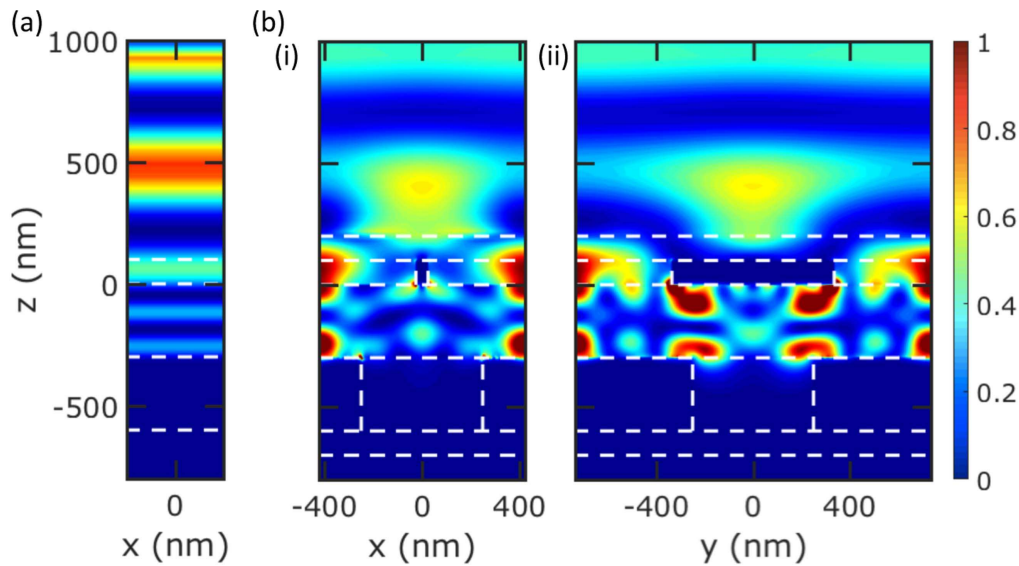
Figure 11. Normalized electric field intensity profiles at incident wavelength $\lambda = 1004$ nm for ultrathin c-Si film with (a) 100 nm Si_3N_4 topside antireflection layer and 300 nm backside Ag, and (b) optimal NM sandwich with a 100 nm Si_3N_4 ARC sitting on a 100 nm thick Ag back mirror. The cross-sectional views for the structure in (i) the x–z plane with $y = 0$, and (ii) the y–z plane with $x = 0$. The electric field profiles are the averaged result from incident light with polarization along x- and y-directions. The dashed white lines indicate the edges of the ARC, c-Si thin film, and back Ag thin film in figure (a); and the edges of ARC, frontside Al NM, c-Si thin film, backside Ag NM, and Ag mirror in (b). (From top to the bottom of the plots.)
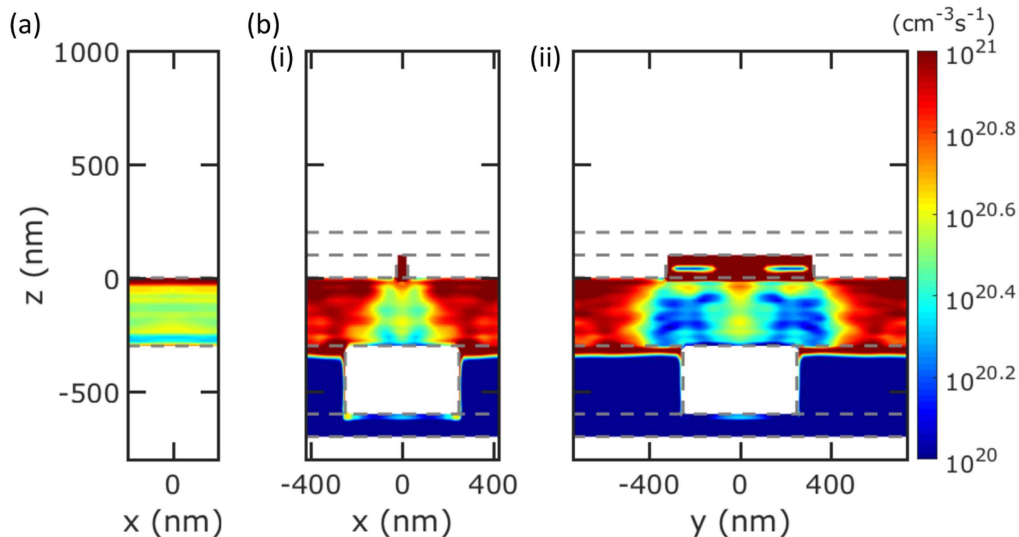
Figure 12. Photocarrier generation rate profiles weighted by the photon flux of the AM1.5 solar spectrum for (a) a bare ultrathin c-Si film and (b) c-Si film with the optimal NM sandwich, Si_3N_4 ARC, and a 100 nm thick Ag back mirror. The cross-sectional views for the structure in (i) the x–z plane with $y = 0$, and (ii) the y–z plane with $x = 0$. The generation rate profiles are the averaged result from incident light with polarization along x- and y-directions under the assumption of unity internal quantum efficiency for photons with an energy above the band gap. The dashed gray lines indicate the edges of the ARC, c-Si thin film, and back Ag thin film in figure (a); and the edges of ARC, frontside Al NM, c-Si thin film, backside Ag NM, and Ag mirror in (b). (From top to the bottom of the plots.)

holes of the metal NM. Figure 7(b) plots the absorption enhancement $g(\lambda)$ between the two structures shown in figure 7(b). The guided modes contribute to the absorption enhancement in the long wavelength regime ($\lambda =$ 700–1100 nm). An over 10-fold enhancement is observed near $\lambda = 796$ nm and 1046 nm.

Figure 8 plots the electric field intensity at (I) $\lambda = 648$, (II) 764, and (III) 1046 nm. The electric field intensity is plotted at these wavelengths for a Si thin film with (a) 300 nm

Ag thin film and (b) optimal Ag NM back reflector. The electric field intensity profiles shown in figure 8(II)(b) and (III)(b) indicate the excitation of leaky waveguide modes. The absorption enhancement at $\lambda = 648$ nm is due to the excitation of a cavity mode (or localized waveguide resonance near its cutoff wavelength) within the cylindrical holes of the metal NMs [42]. This resonance is independent of metal NM pitch. At $\lambda = 764$ and 1046 nm, the incident light is coupled into $(p, q) = (2, 2)$ or $(-2, -2)$ TM waveguide modes.

3.3. NM sandwich optimization

Finally, we explore the combination of a metal NM on both the top and bottom of the ultrathin c-Si film. In addition to the parameters discussed previously, we further consider the spatial offset between the NMs. The frontside NM is Al and backside NM is Ag as simulated before. In addition, the backside metal NM sits on top of a 100 nm thick Ag back reflector like in the previous structure optimized. The optimized NM sandwich consists of a frontside Al NM and a backside Ag NM with $a_{top} = a_{bot} = 850$ nm, $d_{top} = 800$ nm, $t_{top} = 100$ nm, $d_{bot} = 500$ nm, $t_{bot} = 300$ nm, $u = 425$ nm, and $v = 0$. The short-circuit current density of this structure is $J_{sc} = 13.3$ mA cm^{-2}, with $J_{sc,xx} = 13.6$ mA cm^{-2} and $J_{sc,yy} = 13.0$ mA cm^{-2} corresponding to a 41.5% and 20.7% enhancement compared to c-Si with ARC /Ag back reflector and an ideal double pass 300 nm c-Si, respectively. Figure 9 plots the (a) absorption spectra of the optimized NM sandwich compared to c-Si film with ARC and Ag back reflector, and (b) the enhancement in absorption. The enhancement in J_{sc} induced by the NM sandwich is similar to the accumulated enhancement by NM on frontside and backside separately, implying a weak coupling between the SPP near the frontside and the leaky waveguide modes.

The absorption enhancement at long wavelength regime predominantly contributes to the total enhancement, as shown in 9(a). The guided TE and TM waveguide modes for free-standing c-Si with up to $|p|$ and $|q| = 2$ are analytically calculated and plotted in figure 9(a) as well with blue dashed lines near the x-axis. Similarly, the SPP modes with up to $|m|$ and $|n| = 3$ are analytically calculated for the frontside Al and c-Si and plotted with cyan dotted lines near the x-axis. The combination of concentrated electric field intensity from the SPPs excited by the frontside Al NM and the excitation of waveguide modes from the backside Ag NM lead to to high absorption peaks compared with just the frontside or backside NMs alone.

To reduce reflection, an additional silicon nitride Si_3N_4 ARC is used at the frontside. A flat layer of Si_3N_4 with thickness t_{ARC} is positioned upon the frontside NM with the holes in the NM also filled with Si_3N_4. The optimal structure includes an additional Si_3N_4 thin film of thickness $t_{ARC} = 100$ nm added to the former structure. The short-circuit current density of this structure is $J_{sc} = 16.25$ mA cm^{-2}, with $J_{sc,xx} = 16.6$ mA cm^{-2} and $J_{sc,yy} = 15.9$ mA cm^{-2}, as shown in figure 10, corresponding to a 72.9% and 47.8% enhancement compared to c-Si film with ARC and Ag back reflector, and an ideal double pass 300 nm thick c-Si thin film, respectively. By the incorporation of ARC, a broadband absorption enhancement is achieved. The sheet resistance of the Al NM as the top electrode is $R_s = 2.4$ Ω/sq at $T_{solar} = 81\%$, satisfying the industry standard $R_s < 10$ Ω/sq. Table 2 summarizes the short-circuit current density results for these NM structures.

Figure 11 depicts the electric field intensity at free space wavelength $\lambda = 1004$ nm for a 300 nm thick ultrathin c-Si film with (a) 100 nm Si_3N_4/300 nm Ag, and (b) optimal NM sandwich with a 100 nm Si_3N_4 ARC and a 100 nm thick Ag

back mirror. A hybrid of SPP mode and waveguide mode with reduced reflection occurs at this wavelength, corresponding to a 15-folding enhancement in absorption compared with the ARC/c-Si/back Ag structure shown in figure 11(a).

Figure 12 depicts the photocarrier generation rate profiles of the (a) bare ultrathin c-Si film and (b) c-Si film with optimal double-sided NMs. The generation rate profiles are determined from the generation rates at various wavelengths weighted by the photon flux of the AM1.5 solar spectrum at these wavelengths. As shown in figure 12(b), pronounced enhancement in generation rate is demonstrated in the c-Si region with the incorporation of the NM sandwich compared to bare c-Si, despite some parasitic generation in the metal NMs. Unlike that the carrier generation in the c-Si thin film is highest at the front surface, the carrier generation is more in the center of the c-Si thin film with the incorporation of NM sandwich, such that carriers are less likely to be affected by surface recombination. Furthermore, the carrier generation is more uniform within the c-Si, such that photoexcited carriers are less likely to recombine, since the recombination rate is directly proportional to the local excess concentration of electrons and holes.

4. Conclusion

We systematically investigate metal NMs for light trapping in ultrathin c-Si film solar cells. The frontside NM excites SPPs and couples incident light into waveguide modes in the c-Si. The backside NM supports resonances amplified by localized surface plasmons at the metal/c-Si interface. The effect of NMs on either side leads to significant absorption enhancement in c-Si layer in long wavelength regime. To achieve a broadband enhancement, Si_3N_4 is used as ARC to increase the absorption in c-Si in short wavelength regime. We illustrated how metal NM sandwich with appropriate ARC may be utilized to achieve a broadband light trapping with a 72.9% enhancement in short-circuit current compared with that of a 300 nm thick c-Si thin film solar cell with ARC and Ag back reflector.

References

[1] Brendel R, Bergmann R B, Lölgen P, Wolf M and Werner J H 1997 Ultrathin crystalline silicon solar cells on glass substrates *Appl. Phys. Lett.* **70** 390–2

[2] Yoon J *et al* 2008 Ultrathin silicon solar microcells for semitransparent, mechanically flexible and microconcentrator module designs *Nat. Mater.* **7** 907–15

[3] Wang S, Weil B D, Li Y, Wang K X, Garnett E, Fan S and Cui Y 2013 Large-area free-standing ultrathin single-crystal silicon as processable materials *Nano. Lett.* **13** 4393–8

[4] Fang X, Li Y, Wang X, Ding J and Yuan N 2015 Ultrathin interdigitated back-contacted silicon solar cell with light-trapping structures of si nanowire arrays *Sol. Energy* **116** 100–7

[5] Branham M S, Hsu W C, Yerci S, Loomis J, Boriskina S V, Hoard B R, Han S E and Chen G 2015 15.7% efficient 10 μm thick crystalline silicon solar cells using periodic nanostructures *Adv. Mater.* **27** 2182–8

[6] He J, Yang Z, Liu P, Wu S, Gao P, Wang M, Zhou S, Li X, Cao H and Ye J 2016 Enhanced electro-optical properties of nanocone/nanopillar dual-structured arrays for ultrathin silicon/organic hybrid solar cell applications *Adv. Energy Mater.* **6** 1501793

[7] Yablonovitch E 1982 Statistical ray optics *J. Opt. Soc. Am.* **72** 899–907

[8] Yu Z, Raman A and Fan S 2010 Fundamental limit of nanophotonic light trapping in solar cells *Proc. Natl Acad. Sci. USA* **107** 17491–6

[9] Yablonovitch E and Cody G 1982 Intensity enhancement in textured optical sheets for solar cells *IEEE Trans. Electron Devices* **29** 300–5

[10] Catchpole K R 2007 A conceptual model of the diffuse transmittance of lamellar diffraction gratings on solar cells *J. Appl. Phys.* **102** 013102

[11] Schaadt D M, Feng B and Yu E T 2005 Enhanced semiconductor optical absorption via surface plasmon excitation in metal nanoparticles *Appl. Phys. Lett.* **86** 063106

[12] Pillai S, Catchpole K R, Trupke T and Green M A 2007 Surface plasmon enhanced silicon solar cells *J. Appl. Phys.* **101** 093105

[13] Gao T, Stevens E, Lee J K and Leu P W 2014 Designing metal hemispheres on silicon ultrathin film solar cells for plasmonic light trapping *Opt. Lett.* **39** 4647–50

[14] Zhang Y, Stokes N, Jia B, Fan S and Gu M 2014 Towards ultra-thin plasmonic silicon wafer solar cells with minimized efficiency loss *Sci. Rep.* **4** 4939

[15] Catchpole K R and Polman A 2008 Design principles for particle plasmon enhanced solar cells *Appl. Phys. Lett.* **93** 191113

[16] Hägglund C, Zäch M, Petersson G and Kasemo B 2008 Electromagnetic coupling of light into a silicon solar cell by nanodisk plasmons *Appl. Phys. Lett.* **92** 053110

[17] Villesen T F, Uhrenfeldt C, Johansen B, Hansen J L, Ulriksen H U and Larsen A N 2012 Aluminum nanoparticles for plasmon-improved coupling of light into silicon *Nanotechnology* **23** 085202

[18] Cai B, Jia B, Shi Z and Gu M 2013 Near-field light concentration of ultra-small metallic nanoparticles for absorption enhancement in a-Si solar cells *Appl. Phys. Lett.* **102** 093107

[19] Pala R A, White J, Barnard E, Liu J and Brongersma M L 2009 Near-field light concentration of ultra-small metallic nanoparticles for absorption enhancement in a-Si solar cells *Adv. Mater.* **21** 3504–9

[20] Grandidier J, Callahan D M, Munday J N and Atwater H A 2011 Light absorption enhancement in thin-film solar cells using whispering gallery modes in dielectric nanospheres *Adv. Mater.* **23** 1272–6

[21] Wang B and Leu P W 2015 High index of refraction nanosphere coatings for light trapping in crystalline silicon thin film solar cells *Nano Energy* **13** 226–32

[22] Wang B, Gao T and Leu P W 2016 Broadband light absorption enhancement in ultrathin film crystalline silicon solar cells with high index of refraction nanosphere arrays *Nano Energy* **19** 471–5

[23] Ferry V E, Sweatlock L A, Pacifici D and Atwater H A 2008 Plasmonic nanostructure design for efficient light coupling into solar cells *Nano Lett.* **8** 4391–7

[24] Wang W, Wu S, Reinhardt K, Lu Y and Chen S 2010 Broadband light absorption enhancement in thin-film silicon solar cells *Nano Lett.* **10** 2012–8

[25] Ferry V E, Verschuuren M A, Li H B T, Schropp R E I, Atwater H A and Polman A 2009 Improved red-response in thin film a-Si:H solar cells with soft-imprinted plasmonic back reflectors *Appl. Phys. Lett.* **95** 183503

[26] Corcoran C J, Kang S, Li L, Guo X, Chanda S and Nuzzo R G 2013 Mechanisms of enhanced optical absorption for ultrathin silicon solar microcells with an integrated nanostructured backside reflector *ACS Appl. Mater. Interfaces* **5** 4239–46

[27] Rowell M W and McGehee M D 2011 Transparent electrode requirements for thin film solar cell modules *Energy Environ. Sci.* **4** 131–4

[28] Gao T, Wang B, Ding B, Lee J K and Leu P W 2014 Uniform and ordered copper nanomeshes by microsphere lithography for transparent electrodes *Nano Lett.* **14** 2105–10

[29] Gao T, Huang P S, Lee J K and Leu P W 2015 Hierarchical metal nanomesh/microgrid structures for ordered and uniform transparent electrodes *RSC Adv.* **5** 70713–7

[30] Gao H, Henzie J, Lee M H and Odom T W 2008 Screening plasmonic materials using pyramidal gratings *Proc. Natl Acad. Sci. USA* **105** 20146–51

[31] Ferry V E, Munday J N and Atwater H A 2010 Design considerations for plasmonic photovoltaics *Adv. Mater.* **22** 4794–808

[32] Genet C and Ebbesen T W 2007 Light in tiny holes *Nature* **445** 39–46

[33] Yee K 1966 Numerical solution of initial boundary value problems involving Maxwell's equations in isotropic media *IEEE Trans. Antennas Propag.* **14** 302–7

[34] Zivanovic S, Yee K and Mei K 1991 A subgridding method for the time-domain finite-difference method to solve Maxwell's equations *IEEE Trans. Microw. Theory Tech.* **39** 471–9

[35] Palik E D 1997 *Handbook of Optical Constants of Solids* (New York: Academic)

[36] Philipp H R 1973 Optical properties of silicon nitride *J. Electrochem. Soc.* **120** 295–300

[37] Solar spectral irradiance: air mass 1.5 (http://rredc.nrel.gov/solar/spectra/am1.5/)

[38] Pozar D M 2009 *Microwave Engineering* (New York: Wiley)

[39] Johnson S G, Fan S, Villeneuve P R, Joannopoulos J D and Kolodziejski L A 1999 Guided modes in photonic crystal slabs *Phys. Rev.* B **60** 5751–8

[40] Ma W Y, Yang H, Hilton J P, Lin Q, Liu J Y, Huang L X and Yao J 2010 A numerical investigation of the effect of vertex geometry on localized surface plasmon resonance of nanostructures *Opt. Express* **18** 843–53

[41] Maier S A 2007 *Plasmonics: Fundamentals and Applications* (Berlin: Springer)

[42] Ruan Z and Qiu M 2006 Enhanced transmission through periodic arrays of subwavelength holes: The role of localized waveguide resonances *Phys. Rev. Lett.* **96** 233901